Title: Oxygen vacancy ordering in aluminous bridgmanite in the Earth's lower mantle
Author: Helen Grüninger, Zhaodong Liu, Renée Siegel, Tiziana Boffa Ballaran, Tomoo Katsura, Jürgen Senker, Daniel J. Frost
Publication: Geophysical Research Letters
Publisher: American Geophysical Union
Date: 19 July 2019

Oxygen vacancy ordering in aluminous bridgmanite in the Earth's lower mantle

Helen Grüninger[a], Zhaodong Liu[b], Renée Siegel[a], Tiziana Boffa Ballaran[b], Tomoo Katsura[b], Jürgen Senker[a]*, Daniel J. Frost[b]*

[a] Inorganic Chemistry III, University of Bayreuth, Universitätsstr. 30, 95447 Bayreuth, Germany.

[b] Bayerisches Geoinstitut, University of Bayreuth, Universitätsstr. 30, 95447 Bayreuth, Germany.

*Corresponding authors: dan.frost@uni-bayreuth.de, juergen.senker@uni-bayreuth.de

ORCID identifier:

Helen Grüninger: 0000-0002-5422-7003; Tomoo Katsura: 0000-0001-7857-5101;

Jürgen Senker: 0000-0002-7278-7952; Daniel Frost: 0000-0002-4443-8149

Key Points:

- Al substitution in bridgmanite is dominated by the oxygen vacancy mechanism for peridotite mantle compositions
- Short-range ordering of oxygen vacancies takes place forming oxygen vacancy clusters possibly due to migration into twin domain walls
- Oxygen vacancy clusters are expected to have a major influence on transport properties of the lower mantle, such as the electrical conductivity

Abstract Oxygen vacancies (OVs), that charge-balance the replacement of octahedrally coordinated Si^{4+} by Al^{3+} in the mineral bridgmanite, will influence transport properties in the lower mantle but little is known about their stability and local structure. Using ^{27}Al nuclear magnetic resonance (NMR) spectroscopy we have characterized OVs within six aluminous bridgmanite samples. In the resulting NMR spectra six-, five -, and four -fold coordinated Al species are resolved, in addition to near eight-fold coordinated Al substituting for Mg. Five-fold coordinated Al is formed by single OV sites but four-fold coordination must result from short range ordering of OVs, producing OV clusters that may form through migration into twin domain walls. Characterizing the occurrence of such OV structures is an important prerequisite for understanding how transport properties change with depth and composition in the lower mantle.

Plain language summary The lower mantle encompasses the largest region of the Earth's interior and is mainly composed of the perovskite-structured mineral $(Mg,Fe)(Al,Si)O_3$ bridgmanite. Its properties, therefore, control both the diffusive transport of elements and solid state flow in the lower mantle, which will be strongly influenced by point defects. We have identified and quantified defects in bridgmanite that arise from the replacement of silicon by aluminum and result in the creation of a vacant oxygen site. These oxygen defects are also found to form clusters in the structure, which in other perovskite structured minerals have been shown to strongly affect physical properties. As defect formation and ordering is dependent on composition and pressure, strong variations in physical properties may be expected within the upper 300 km of the lower mantle.

1. Introduction

In order to understand transport properties such as creep and electrical conductivity in the lower mantle it is important to characterize the nature of the determinant point defects in the dominant lower mantle mineral bridgmanite, which occur mainly as a result of the substitution of trivalent cations (Kurnosov et al., 2017; Manthilake et al., 2011; C. McCammon, 1997; Navrotsky, 1999; Xu & McCammon, 2002). Perovskite structured $MgSiO_3$ bridgmanite contains Si in octahedral coordination (B site substitution) and Mg occupying a larger dodecahedral site (A site substitution). Al is the most abundant trivalent cation substituting into bridgmanite, followed by Fe^{3+} (Lauterbach et al., 2000; C. McCammon, 1997), and can be incorporated either by substituting for Si, with charge balance provided through the formation of oxygen vacancies (OVs), or by the coupled substitution of Mg and Si by 2 Al. The former mechanism is characterized by the fictive endmember $MgAlO_{2.5}$ and is expected to be favored in bulk pyrolitic mantle compositions where the presence of ferropericlase, (Mg,Fe)O renders a low silica activity (Brodholt, 2000; Navrotsky, 1999). The latter charge coupled (CC) mechanism should dominant in Al_2O_3- or SiO_2-rich systems as well as in the deeper portions of the lower mantle (Brodholt, 2000; Liu et al., 2017a; Liu et al., 2017b). The two mechanisms should have different impacts on the elastic properties, diffusivity, conductivity and rheology of bridgmanite. Oxygen mobility in ceramic perovskites studied for fuel

cell applications, for example, has been shown to be controlled by the concentration of OVs (Navrotsky, 1999) and the mobility of protons in bridgmanite may be similarly controlled, even if the absolute solubility remains low (Bolfan-Casanova et al., 2000; Navrotsky et al., 2003). As in ceramic perovskites, changes in the transport properties of bridgmanite will likely also depend on the local distribution of OVs in the structure (Klie et al., 2001; Kruidhof et al., 1993). In many perovskites progressive ordering of OVs occurs with increasing trivalent cation substitution, from locally ordered dimer and trimer clusters, to extended chains and ultimately to planes with long range ordering, such as in the end member $Ca(Al,Fe)O_{2.5}$ brownmillerite (Becerro et al., 1999). Changes in OV ordering are also linked to changes in transport properties such as electrical conductivity and oxygen diffusivity (Figueiredo et al., 2003; Zhang & Smyth, 1995). To date, however, no evidence for OV ordering in bridgmanite has been reported and even the occurrence of OVs has been mainly implied through chemical analyses. X-ray absorption and NMR spectroscopic studies of the local structure around the Al atoms in bridgmanite have identified Al in six-fold or higher coordination (Andrault et al., 1998; Palke et al., 2012; Stebbins et al., 2001,

2003), consistent with the CC mechanism, although Stebbins et al., (2006) observed an Al B to A ratio of 2:1 in one sample of bridgmanite from which the formation of OVs was implied.

Recent high pressure experiments, which have used chemical compositions to infer the existence of OVs in Al-bearing bridgmanite, imply that they are stabilized in MgO-saturated bulk compositions with increasing temperature (Liu et al., 2019) but decrease in abundance with both increasing Al contents (> 0.1 Al atoms per $MgSiO_3$ formula unit, henceforth, pfu) and pressure (Liu et al., 2017a; Liu et al., 2017b). Although these conditions are consistent with OVs being important at the top of the lower mantle and are likely to be the most abundant type of vacancy defect in the entire mantle, the conditions where the OV mechanism dominates over the CC mechanism are sensitive to the pressure, temperature and chemical composition and have likely been overlooked in many previous experimental studies.

Here we report the first detection of ordering of OVs in Al-bearing bridgmanite using an analysis of ^{27}Al magic angle spinning (MAS) NMR spectra. A suit of bridgmanite samples were synthesized over a range of Al contents and SiO_2 activities designed to explore the extent of OV formation. To clarify the type and ratio of the Al species within bridgmanite, DFT calculations for various CC and OV defect configurations were combined with a quantitative analysis of ^{27}Al MAS NMR spectra for all samples. For the interpretation of the ^{27}Al NMR spectra we rely on identifying

the characteristic lineshapes for the Al species based on reference spectra where the different Al substitution mechanisms, OV and CC are at a maximum. 2D ^{27}Al satellite-transition MAS spectroscopy (STMAS) was also employed to increase the spectral resolution. We provide direct evidence for the formation of OVs, their concentration and ordering as a function of bridgmanite composition and show that they should dominate the Al substitution mechanism in the upper region of the lower mantle and thereby exert an important influence on transport properties.

2. Materials and Methods

Six Al-bearing bridgmanite samples were investigated in this study: three samples were synthesized along the join $MgSiO_3$–$MgAlO_{2.5}$ and two along the join $MgSiO_3$–Al_2O_3 (Table 1) using a multi-anvil apparatus (Ishii et al., 2016). To ensure chemical homogeneity vitreous (glassed) starting materials were employed. A further bridgmanite sample was synthesized from a starting material comprised of 70 wt% of enstatite containing 5 mol% of Al_2O_3 and 30 wt% of MgO (sample F). All samples were recovered from the high-pressure high-temperature runs in the form of well-sintered pellets, which were analyzed without being ground to a powder in order to avoid amorphization.

Characterization was performed by means of scanning electron microscopy (Fig. S1) and powder X-ray diffraction (Fig. 1). The samples comprised either monomineralic bridgmanite or bridgmanite plus MgO or Al_2O_3 (Table 1). The proportions of the stoichiometric CC and OV components present in the synthesized Al-bearing bridgmanites (Table 1) were estimated from their compositions, as measured by electron probe micro analyzer (EPMA, Table S3), according to the following expression:

$$Mg_xAl_zSi_yO_{x+1.5z+2y}\ (Brg) = y\ MgSiO_3 + (x-y)\ MgAlO_{2.5}\ (OV) + (z-x+y)/2\ AlAlO_3\ (CC) \quad (1)$$

Quantitative 1D ^{27}Al MAS NMR spectra (Kentgens, 1991) were acquired to probe the local Al environment within bridgmanite (Fig. 1). Furthermore, for sample B a 2D ^{27}Al STMAS spectrum (Kwak & Gan, 2003; Siegel et al., 2009) was recorded to enhance the resolution and to identify the spectral lineshape of the individual Al defect sites (Fig. 2). 1D ^{27}Al MAS NMR echo spectra of sample A and B were recorded at a higher magnetic field of 23.5 T (Fig. S4) to corroborate the results of the quantitative analysis. DFT calculations of multiple Al defect structures were used to determine the expected NMR parameters for different scenarios of the CC and OV substitution mechanism. The simulations were carried out using the CASTEP DFT code (Charpentier, 2011; Clark et al., 2005; Grimme, 2006; Perdew et al., 1996; Pickard & Mauri, 2001; Profeta et al., 2003; Yates et al., 2007). Details on synthesis conditions, DFT calculations and characterization methods are summarized in the SI.

3. Results

^{27}Al MAS NMR spectra were collected on six Al-bearing bridgmanite samples (A to F; Figure 1). All spectra show a sharp resonance at ~7 ppm, corresponding to Al in a symmetric octahedral environment, and a broad signal with a maximum at ~-20 ppm, indicating a larger coordination number and a distorted environment for the Al species. In accordance with the literature these signals are assigned to Al on the B and the A site, respectively, (Palke et al., 2012; Stebbins et al., 2001, 2003, 2006) and can be explained by the CC substitution mechanism. The NMR spectra of samples E and C exhibit an additional signal (~15 ppm) corresponding to corundum (Palke et al., 2012; Stebbins et al., 2006), which is consistent with the XRD phase analysis (Fig. 1, left). However, in the spectra of samples A-C and F broad and overlapping resonances in the typical shift range of tetra- and penta-coordinated Al (^{IV}Al, ^{V}Al) were observed (Choi et al., 2009; MacKenzie & Smith, 2002; Smith, 1993).

While BSE images and the XRD analysis provide no evidence for the presence of amorphous materials, we cannot rule out the existence of small amounts of glassy materials based on these measurements alone. Previous studies, however, demonstrate the crystallization of $MgSiO_3$ glass even at 1100 K (Ono et al., 2017) at similar pressures, so the initial starting material glass must have fully crystalized during the experiment. Although it is possible that minor amounts of H_2O adsorbed onto the starting materials could have induced small degree melting of the sample, such

a melt is not expected to be enriched in Al based on measured bridgmanite-melt partition coefficients (Corgne et al., 2005; Liebske et al., 2005) and, therefore, the NMR signal would be very weak. Furthermore, such a melt would likely contain ^{VI}Al rather than ^{IV}Al and ^{V}Al species (Allwardt et al. 2005) and would crystalize on quenching. As a consequence we can be quite certain that the observed ^{IV}Al and ^{V}Al signals are a characteristic feature of Al defects in Al-bearing bridgmanite.

To develop a microscopic understanding of the CC and OV incorporation mechanisms as a function of the synthesis conditions, we extracted the ratios of ^{IV}Al, ^{V}Al, ^{VI}Al species and Al on the A site (^{A}Al) by a quantitative deconvolution of the ^{27}Al NMR spectra (Tab. S4, Fig. S3). For this, two reference samples (D and B) were selected in order to assign a characteristic spectral lineshape to each individual Al environment. The EPMA results for sample D imply mainly CC defects (Tab. 1) and its ^{27}Al NMR spectrum could be refined with two Al resonances typical for Al on the A and B sites (Fig. S2), in agreement with previous results (Stebbins et al., 2003, 2006). Both the chemical shift (δ_{iso}) and the quadrupolar coupling interaction (C_Q) and asymmetry parameter (η_Q) show a distribution consistent with disorder of the bond distances, angles and second-neighbor cations around the Al defects in the bridgmanite structure. The relevant refinement parameters are summarized in Table S4.

The EPMA analyses for sample B indicate that it has the highest stoichiometric OV component (Tab. 1) and thus offers the best opportunity to identify spectral lineshapes for Al environments influenced by OVs. This was achieved using a 2D ^{27}Al STMAS spectrum (Fig. 2, Tab. S4) (Ashbrook & Wimperis, 2004; Gan, 2000; Kwak & Gan, 2003), for which four signals were clearly observed. They confirm the presence of the following four Al environments in bridgmanite: ^{IV}Al, ^{V}Al, ^{VI}Al and ^{A}Al. While Al on the A site (^{A}Al) results from the CC mechanism, ^{IV}Al and ^{V}Al species are a consequence of neighboring OVs. The ^{VI}Al signal appears to have two contributions, one for the B site substitution associated with the CC mechanism and a broader contribution arising from disorder and distortion introduced by OVs. The entire signal intensity is also too high to be accounted for by CC defects alone. These results are also corroborated by ^{27}Al MAS echo spectra (Fig. S4) recorded at a higher magnetic field (23.5 T).

To support the assignment of the ^{27}Al NMR spectra, quantum-mechanical calculations for a number of Al defect models were performed to determine values expected for the NMR parameters δ_{iso}, C_Q and η_Q (Table S6). For the CC substitution mechanism two defect models were calculated (Fig. 3a, b), in which one Mg is substituted by Al (A site) and one Si is replaced by Al either at the nearest-neighbor or at the next nearest-neighbor B site (Fig. 3a, b). For the OV substitution mechanism in total 12 models were considered in order to take into account the possible formation of isolated oxygen vacancies (Fig. 3c, Fig. S5), as well as the formation of OV dimers (Fig. 3d-f,

Fig. S6 to S8). Isolated oxygen vacancies shared between two B sites result in the formation of penta-coordinated Al species (Fig 3c, Fig. S5), even when clustering linearly on two adjacent octahedra (Fig. 3d, Fig. S6). However, in order to form tetrahedral Al^{3+} in the bridgmanite structure, short range ordering of OVs must occur, as observed, for example, in Fe^{3+}-bearing $CaTiO_3$ perovskite (Fig. 3e, Fig. S7 to S8) (Becerro et al., 1999; McCammon et al., 2000). If two neighboring OVs within one octahedron are created, tetrahedral, octahedral and two pentagonal Al environments are formed (Fig. 3e). A further model that was tested is where one Al and one Si occupy the penta-coordinated sites (Fig. 3f, Fig. S8) and charge balance is maintained by a further Al occupying an octahedral site. In this configuration one ^{VI}Al is not directly associated with the OVs, a possibility that has been proposed previously (Stebbins et al., 2006), which could result, for example, from OV migration. Assuming that combinations of all configurations are possible, for each tetrahedrally coordinated Al either one or two penta-coordinated and octahedral Al sites arise. As a consequence, the intensity ratio cannot be unambiguously linked to one individual configuration for OV short-range order.

The calculated NMR parameters for the CC models (Fig. 3a, b) are in very good agreement with the experimental values of the signals observed in sample D (Fig. 3g). This corroborates the signal assignment of Al on the A and B sites depicted in Figure 2. While CC models including migration of Al within the structure exhibit slightly larger energies (ΔE ~10 $kJmol^{-1}$), the calculated NMR

parameters for all models are quite close to each other (Table S6). As a consequence, we consider both scenarios to be in agreement with the results of the NMR analysis (Fig. 3g).

For all considered OV defect models the simulated isotropic chemical shift and quadrupolar coupling constants agree reasonably well with the experimentally obtained values (Fig. 3g, Table S6). For the ^{IV}Al species an overestimation of the simulated values of about ΔC_Q =3 MHz and $\Delta\delta_{iso}$=10 ppm occurred, which we attribute to stronger distortions in the simulations (0 K and ambient pressure), the tendency of DFT calculations to overestimate the electric field gradient (EFG) tensor (Martineau et al., 2014) and to the observed distributions for the chemical shift and quadrupolar coupling values (Table S4).

In particular, the occurrence of tetrahedrally coordinated Al demonstrates the presence of OV clusters comparable to Fig. 3e and f due to short-range ordering. In the case of the octahedral Al environments, the NMR parameters of those defects not directly associated with OVs fit the experimental data slightly better. This supports the migration of OVs, and is potentially consistent with a high mobility of oxygen ions at the synthesis conditions. As a consequence, they exhibit a very similar spectral signature compared to octahedral sites created by the CC substitution mechanism.

4. Discussion

The 1D ^{27}Al MAS NMR spectra were deconvoluted using the characteristic parameters for each type of Al coordination (Tab. 2, Fig. S3), to obtain the relative intensities of each Al environment (Tab. S5). We use the relative integral of the A site resonance as a measure for Al incorporated due to the CC mechanism, since it is well separated from the other resonances. The same relative intensity is then subtracted from the total ^{VI}Al intensity according to the stoichiometry of the CC mechanism. The remaining ^{VI}Al intensity is then combined with the intensities of ^{V}Al and ^{IV}Al to determine the relative proportion of the OV component. The resulting OV/CC ratios are in good agreement with those estimated from compositional analyses (Tab. 2), within the analytical uncertainties.

The OV substitution mechanism initially dominates in Al bearing bridgmanites coexisting with MgO along the $MgSiO_3$–$MgAlO_{2.5}$ join, and increases with Al content to a maximum in OV component at ~ 0.1 Al pfu. (Fig. 4a, Table S5), after which the CC substitution, which also increases with increasing Al content becomes dominant. The presence of ^{IV}Al, even in the lowest Al-bearing sample, however, indicates that there must be partial ordering of OVs, to a degree which appears to decrease with increasing Al-content (Fig. 4b grey, Table S5). The absolute concentrations of ^{IV}Al and ^{V}Al, however, remain relatively constant up to sample C (~ 0.1 Al pfu.), implying a similar level of partial ordering is maintained until the CC mechanism starts to take over.

Bridgmanites synthesized with coexisting corundum along the $MgSiO_3$–Al_2O_3 join, have a limited OV component and are instead dominated by the CC mechanism (Fig. 4a). Note that the bridgmanite sample F, contains a significantly higher OV component than sample D, which was produced from the same nominal composition in the absence of excess MgO. This clearly demonstrates that the presence of MgO favors the OV substitution mechanism as it buffers the SiO_2-activity at the lowest level. In a peridotite composition lower mantle, bridgmanite coexists with MgO-rich ferropericlase and the OV mechanism should, therefore, dominate. Although bridgmanite in the lower mantle is expected to contain some Fe^{3+}, which occupies the A-site and forms a stable CC mechanism with ^{VI}Al, the proportion of Fe^{3+} should be insufficient to balance all Al in this way (Frost et al., 2004; Shim et al., 2017), and compositional evidence indicates that OVs are also present in Fe- and Al-bearing bridgmanite (Frost & Langenhorst, 2002; Lauterbach et al., 2000).

When bridgmanite forms in down welling peridotite material at the top of the lower mantle it will contain little Al, which partitions strongly into coexisting majoritic garnet at these conditions (Irifune, 1994). With increasing depth, garnet breaks down and the Al content of bridgmanite increases. At depths of approximately 720 km, the OV component in bridgmanite should reach a maximum, but it appears that with a further increase in pressure the OV mechanism becomes less favorable (Brodholt, 2000), and compositional analyses infer that it reaches negligible proportions

at depths below 1000 km (Liu et al., 2017a; Liu et al., 2017b). In contrast, in basaltic segments of subducting slabs the larger Al_2O_3 content with respect to the ambient mantle will suppress OV formation and favor the CC mechanism for bridgmanite Al substitution. As the formation of OVs is compositionally dependent, lateral variations in their concentration and state of ordering can be expected in the top of the lower mantle, in addition to a gradual decline between depths of 800 to 1000 km.

A number of transport properties in addition to the partitioning of H_2O and noble gases are likely linked to the abundance of OVs and their local ordering. Studies of ceramic perovskites have shown that the structural arrangement of OVs have important effects on transport properties. Based on measurements made on the analogous perovskite $LaAlO_3$, it has been proposed that the motion of twin domain walls could be a source of seismic wave attenuation in the lower mantle (Harrison & Redfern, 2002). Twin domains, however, were found to become pinned at low temperatures, which was postulated to be caused by OVs that migrate to the twin domain wall. Computer simulations have confirmed that it is energetically favorable for OVs to reside in twin walls (Calleja et al., 2003), raising the intriguing possibility that the partial ordering observed in this study might arise from OV clusters that have migrated to the walls of twin domain, as similar multiple twins are also observed in bridgmanite (Wang et al., 1992). Seismic attenuation in the lower mantle may therefore depend critically on the occurrence of clustered OVs. Similarly,

measurements of electrical and ionic conductivity in analogous $CaTiO_3$-$CaFeO_{2.5}$ perovskites have been shown to be strongly dependent on the extent of partial ordering of OVs, because it is coupled to an overall decrease in oxygen mobility (Figueiredo et al., 2003; Zhang & Smyth, 1995)**.** Lateral variability in electrical conductivity inferred for the top of the lower mantle (Deschamps, 2015) might, therefore, be explained by compositionally driven variations in OV concentration and ordering.

Previous studies have proposed that noble gases such as neon and argon, which have relatively high solubilities in bridgmanite, may be accommodated on OV sites, due to their comparable atomic-size (Shcheka & Keppler, 2012; Y. Zhang & Xu, 1995). This may well be facilitated by the much larger cavity and consequent relaxation resulting from OV partial ordering. It has also been proposed that OVs may be suitable sites for substitution by hydroxyl groups and the possibility has been raised that rapid proton migration could lead to a homogenization of the H_2O content within the lower mantle (Murakami et al., 2012; Navrotsky, 1999). OV partial ordering, particularly if it occurs within twin domain walls, may have an important effect on proton mobility. A broad range of lower mantle geochemical and transport properties are, therefore, likely to be dependent on the occurrence and partial ordering of OVs, which may lead to strong variations in physical properties within the top 300 km of the lower mantle. This may even be consistent with the increase in mantle viscosity inferred by some models towards the mid lower mantle (Ricard &

Wuming, 1991). Numerous studies that have examined bridgmanite physical properties in the past have neglected to buffer the SiO_2 activity and are therefore unlikely to have stabilized OVs in abundances that are realistic for the mantle. Further experiments that pay attention to the role of OV and their local ordering are therefore essential if accurate lower mantle physical and chemical properties are to be determined.

Acknowledgements

H.G. acknowledges the "Fonds der Chemischen Industrie" for financial support in the form of the Chemiefonds Fellowship. All data, including defect models (CIF files), can be found within the manuscript or the supporting information.

Author contributions

H.G., Z.L., T.B.B., J.S. and D.J.F. conceived the study; Z.L. was involved with the high-pressure synthesis, as well as the XRD and EPMA analysis of the samples; H.G. and R.S. performed the solid-state NMR experiments; H.G. conceived and conducted the DFT simulations; all authors analyzed and interpreted the data; H.G., Z.L., T.B.B., J.S. and D.J.F. prepared the manuscript. All authors discussed the results and commented on the manuscript.

References

Allwardt, J. R., Stebbins, J. F., Schmidt, B. C., Frost, D. J., Withers, A. C., & Hirschmann, M. M. (2005). Aluminum coordination and the densification of high-pressure aluminosilicate glasses. *American Mineralogist*, *90*(7), 1218–1222. https://doi.org/10.2138/am.2005.1836

Andrault, D., Neuville, D. R., Flank, A. M., & Wang, Y. (1998). Cation sites in Al-rich $MgSiO_3$ perovskites. *American Mineralogist*, *83*(9–10), 1045–1053. https://doi.org/10.2138/am-1998-9-1013

Ashbrook, S. E., & Wimperis, S. (2004). High-resolution NMR of quadrupolar nuclei in solids: the satellite-transition magic angle spinning (STMAS) experiment. *Progress in Nuclear Magnetic Resonance Spectroscopy*, *45*(1–2), 53–108. https://doi.org/10.1016/j.pnmrs.2004.04.002

Becerro, A. I., McCammon, C., Langenhorst, F., Seifert, F., & Angel, R. (1999). Oxygen vacancy ordering in $CaTiO_3$ –$CaFeO_{2.5}$ perovskites: From isolated defects to infinite sheets. *Phase Transitions*, *69*(1), 133–146. https://doi.org/10.1080/01411599908208014

Bolfan-Casanova, N., Keppler, H., & Rubie, D. C. (2000). Water partitioning between nominally anhydrous minerals in the MgO-SiO_2-H_2O system up to 24 GPa: Implications for the distribution of water in the Earth's mantle. *Earth and Planetary Science Letters*, *182*(3–4), 209–221. https://doi.org/10.1016/S0012-821X(00)00244-2

Brodholt, J. P. (2000). Pressure-induced changes in the compression mechanism of aluminous perovskite in the Earth's mantle. *Nature*, *407*(6804), 620–622. https://doi.org/10.1038/35036565

Calleja, M., Dove, M. T., & Salje, E. K. H. (2003). Trapping of oxygen vacancies on twin walls of $CaTiO_3$: a computer simulation study. *Journal of Physics: Condensed Matter*, *15*(14), 2301–2307. https://doi.org/10.1088/0953-8984/15/14/305

Charpentier, T. (2011). The PAW/GIPAW approach for computing NMR parameters: a new dimension added to NMR study of solids. *Solid State Nuclear Magnetic Resonance*, *40*(1), 1–20. https://doi.org/10.1016/j.ssnmr.2011.04.006

Choi, M., Matsunaga, K., Oba, F., & Tanaka, I. (2009). ^{27}Al NMR Chemical Shifts in Oxide Crystals: A First-Principles Study. *The Journal of Physical Chemistry C*, *113*(9), 3869–3873. https://doi.org/10.1021/jp810484j

Clark, S. J., Segall, M. D., Pickard, C. J., Hasnip, P. J., Probert, M. J., Refson, K., & Payne, M.

C. (2005). First principles methods using CASTEP. *Z. Kristall.*, *220*, 567–570.

Corgne, A., Liebske, C., Wood, B. J., Rubie, D. C., & Frost, D. J. (2005). Silicate perovskite-melt partitioning of trace elements and geochemical signature of a deep perovskitic reservoir. *Geochimica et Cosmochimica Acta*, *69*(2), 485–496. https://doi.org/10.1016/j.gca.2004.06.041

Deschamps, F. (2015). Lower Mantle Electrical Conductivity Inferred from Probabilistic Tomography. *Terrestrial, Atmospheric and Oceanic Sciences*, *26*(1), 27–40. https://doi.org/10.3319/TAO.2014.08.19.03(GRT)

Figueiredo, F., Waerenborgh, J., Kharton, V. V., Näfe, H., & Frade, J. R. (2003). On the relationships between structure, oxygen stoichiometry and ionic conductivity of $CaTi_{1-x}Fe_xO_{3-\delta}$ (x=0.05, 0.20, 0.40, 0.60). *Solid State Ionics*, *156*(3–4), 371–381. https://doi.org/10.1016/S0167-2738(02)00762-2

Frost, D. J., & Langenhorst, F. (2002). The effect of Al_2O_3 on Fe–Mg partitioning between magnesiowüstite and magnesium silicate perovskite. *Earth and Planetary Science Letters*, *199*(1–2), 227–241. https://doi.org/10.1016/S0012-821X(02)00558-7

Frost, D. J., Liebske, C., Langenhorst, F., McCammon, C. A., Trønnes, R. G., & Rubie, D. C. (2004). Experimental evidence for the existence of iron-rich metal in the Earth's lower mantle. *Nature*, *428*(6981), 409–412. https://doi.org/10.1038/nature02413

Gan, Z. (2000). Isotropic NMR Spectra of Half-Integer Quadrupolar Nuclei Using Satellite Transitions and Magic-Angle Spinning. *Journal of the American Chemical Society*, *122*(13), 3242–3243. https://doi.org/10.1021/ja9939791

Grimme, S. (2006). Semiempirical GGA-type density functional constructed with a long-range dispersion correction. *Journal of Computational Chemistry*, *27*(15), 1787–1799. https://doi.org/10.1002/jcc.20495

Harrison, R. J., & Redfern, S. A. T. (2002). The influence of transformation twins on the seismic-frequency elastic and anelastic properties of perovskite: dynamical mechanical analysis of single crystal $LaAlO_3$. *Physics of the Earth and Planetary Interiors*, *134*(3–4), 253–272. https://doi.org/10.1016/S0031-9201(02)00190-5

Irifune, T. (1994). Absence of an aluminous phase in the upper part of the Earth's lower mantle. *Nature*, *370*(6485), 131–133. https://doi.org/10.1038/370131a0

Ishii, T., Shi, L., Huang, R., Tsujino, N., Druzhbin, D., Myhill, R., et al. (2016). Generation of

pressures over 40 GPa using Kawai-type multi-anvil press with tungsten carbide anvils. *Review of Scientific Instruments*, *87*(2), 024501. https://doi.org/10.1063/1.4941716

Kentgens, A. P. . (1991). Quantitative excitation of half-integer quadrupolar nuclei by a frequency-stepped adiabatic half-passage. *Journal of Magnetic Resonance*, *95*(3), 619–625. https://doi.org/10.1016/0022-2364(91)90179-W

Klie, R. F., Ito, Y., Stemmer, S., & Browning, N. D. (2001). Observation of oxygen vacancy ordering and segregation in Perovskite oxides. *Ultramicroscopy*, *86*(3–4), 289–302. https://doi.org/10.1016/S0304-3991(00)00120-0

Kojitani, H., Katsura, T., & Akaogi, M. (2007). Aluminum substitution mechanisms in perovskite-type $MgSiO_3$: an investigation by Rietveld analysis. *Physics and Chemistry of Minerals*, *34*(4), 257–267. https://doi.org/10.1007/s00269-007-0144-z

Kruidhof, H., Bouwmeester, H. J. M., v. Doorn, R. H. E., & Burggraaf, A. J. (1993). Influence of order-disorder transitions on oxygen permeability through selected nonstoichiometric perovskite-type oxides. *Solid State Ionics*, *63–65*(02), 816–822. https://doi.org/10.1016/0167-2738(93)90202-E

Kurnosov, A., Marquardt, H., Frost, D. J., Ballaran, T. B., & Ziberna, L. (2017). Evidence for a Fe^{3+}-rich pyrolitic lower mantle from (Al,Fe)-bearing bridgmanite elasticity data. *Nature*, *543*, 543–546. https://doi.org/10.1038/s41586-018-0115-1

Kwak, H.-T., & Gan, Z. (2003). Double-quantum filtered STMAS. *Journal of Magnetic Resonance*, *164*(2), 369–372. https://doi.org/10.1016/S1090-7807(03)00246-5

Lauterbach, S., McCammon, C. A., van Aken, P., Langenhorst, F., & Seifert, F. (2000). Mössbauer and ELNES spectroscopy of $(Mg,Fe)(Si,Al)O_3$ perovskite: a highly oxidised component of the lower mantle. *Contributions to Mineralogy and Petrology*, *138*(1), 17–26. https://doi.org/10.1007/PL00007658

Liebske, C., Corgne, A., Frost, D. J., Rubie, D. C., & Wood, B. J. (2005). Compositional effects on element partitioning between Mg-silicate perovskite and silicate melts. *Contributions to Mineralogy and Petrology*, *149*(1), 113–128. https://doi.org/10.1007/s00410-004-0641-8

Liu, Z., Nishi, M., Ishii, T., Fei, H., Miyajima, N., Ballaran, T. B., et al. (2017a). Phase relations in the system $MgSiO_3$ -Al_2O_3 up to 2300 K at lower mantle pressures. *Journal of Geophysical Research: Solid Earth*, *122*(10), 7775–7788. https://doi.org/10.1002/2017JB014579

Liu, Z., Ishii, T., & Katsura, T. (2017b). Rapid decrease of $MgAlO_{2.5}$ component in bridgmanite with pressure. *Geochemical Perspectives Letters*, *5*, 12–18. https://doi.org/10.7185/geochemlet.1739

Liu, Z., Akaogi, M., & Katsura, T. (2019). Increase of the oxygen vacancy component in bridgmanite with temperature. *Earth and Planetary Science Letters*, 505, 141–151. https://doi.org/10.1016/j.epsl.2018.10.014

MacKenzie, K. J. D., & Smith, M. E. (2002). *Multinuclear Solid-State NMR of Inorganic Materials*. (R. W. Kahn, Ed.), *Pergamon Materials Series* (Volume 6). Oxford: Pergamon.

Manthilake, G. M., de Koker, N., Frost, D. J., & McCammon, C. A. (2011). Lattice thermal conductivity of lower mantle minerals and heat flux from Earth's core. *Proceedings of the National Academy of Sciences*, *108*(44), 17901–17904. https://doi.org/10.1073/pnas.1110594108

Martineau, C., Senker, J., & Taulelle, F. (2014). NMR Crystallography. *Annual Reports on NMR Spectroscopy*, *82*, 1–57. https://doi.org/10.1016/B978-0-12-800184-4.00001-1

McCammon, C. (1997). Perovskite as a possible sink for ferric iron in the lower mantle. *Nature*, *387*(6634), 694–696. https://doi.org/10.1038/42685

McCammon, C. A., Becerro, A. I., Langenhorst, F., Angel, R. J., Marion, S., & Seifert, F. (2000). Short-range ordering of oxygen vacancies in $CaFe_xTi_{1-x}O_{3-x/2}$ perovskites ($0 < x < 0.4$). *Journal of Physics: Condensed Matter*, *12*(13), 2969–2984. https://doi.org/10.1088/0953-8984/12/13/308

Murakami, M., Ohishi, Y., Hirao, N., & Hirose, K. (2012). A perovskitic lower mantle inferred from high-pressure, high-temperature sound velocity data. *Nature*, *485*(7396), 90–94. https://doi.org/10.1038/nature11004

Navrotsky, A. (1999). A Lesson from Ceramics. *Science*, *284*(5421), 1788–1789. https://doi.org/10.1126/science.284.5421.1788

Navrotsky, A., Schoenitz, M., Kojitani, H., Xu, H., Zhang, J., Weidner, D. J., & Jeanloz, R. (2003). Aluminum in magnesium silicate perovskite: Formation, structure, and energetics of magnesium-rich defect solid solutions. *Journal of Geophysical Research: Solid Earth*, *108*(B7), ECV2-1–11. https://doi.org/10.1029/2002JB002055

Ono, S., Kikegawa, T., & Higo, Y. (2017). Reaction boundary between akimotoite and ringwoodite + stishovite in $MgSiO_3$. *Physics and Chemistry of Minerals*, *44*, 425–430.

https://doi.org/10.1007/s00269-016-0869-7

Palke, A. C., Stebbins, J. F., Frost, D. J., & McCammon, C. A. (2012). Incorporation of Fe and Al in $MgSiO_3$ perovskite: An investigation by ^{27}Al and ^{29}Si NMR spectroscopy. *American Mineralogist*, *97*(11–12), 1955–1964. https://doi.org/10.2138/am.2012.4101

Perdew, J. P., Burke, K., & Ernzerhof, M. (1996). Generalized Gradient Approximation Made Simple. *Physical Review Letters*, *77*(18), 3865–3868. https://doi.org/10.1103/PhysRevLett.77.3865

Pickard, C., & Mauri, F. (2001). All-electron magnetic response with pseudopotentials: NMR chemical shifts. *Physical Review B*, *63*(24), 245101. https://doi.org/10.1103/PhysRevB.63.245101

Profeta, M., Mauri, F., & Pickard, C. J. (2003). Accurate first principles prediction of ^{17}O NMR parameters in SiO_2: Assignment of the zeolite ferrierite spectrum. *Journal of the American Chemical Society*, *125*(2), 541–548. https://doi.org/10.1021/ja027124r

Ricard, Y., & Wuming, B. (1991). Inferring the viscosity and the 3-D density structure of the mantle from geoid, topography and plate velocities. *Geophysical Journal International*, *105*(3), 561–571. https://doi.org/10.1111/j.1365-246X.1991.tb00796.x

Shcheka, S. S., & Keppler, H. (2012). The origin of the terrestrial noble-gas signature. *Nature*, *490*(7421), 531–534. https://doi.org/10.1038/nature11506

Shim, S.-H., Grocholski, B., Ye, Y., Alp, E. E., Xu, S., Morgan, D., et al. (2017). Stability of ferrous-iron-rich bridgmanite under reducing midmantle conditions. *Proceedings of the National Academy of Sciences*, *114*(25), 6468–6473. https://doi.org/10.1073/pnas.1614036114

Siegel, R., Rocha, J., & Mafra, L. (2009). Combining STMAS and CRAMPS NMR spectroscopy: High-resolution HETCOR NMR spectra of quadrupolar and 1H nuclei in solids. *Chemical Physics Letters*, *470*(4–6), 337–341. https://doi.org/10.1016/j.cplett.2009.01.053

Smith, M. E. (1993). Application of ^{27}Al NMR techniques to structure determination in solids. *Applied Magnetic Resonance*, *4*(1–2), 1–64. https://doi.org/10.1007/BF03162555

Stebbins, J. F., Kroeker, S., & Andrault, D. (2001). The mechanism of solution of aluminum oxide in $MgSiO_3$ perovskite. *Geophysical Research Letters*, *28*(4), 615–618. https://doi.org/10.1029/2000GL012279

Stebbins, J. F., Kojitani, H., Akaogi, M., & Navrotsky, A. (2003). Aluminum substitution in $MgSiO_3$ perovskite: Investigation of multiple mechanisms by ^{27}Al NMR. *American Mineralogist*, *88*(7), 1161–1164. https://doi.org/10.2138/am-2003-0724

Stebbins, J. F., Du, L.-S., Kelsey, K., Kojitani, H., Akaogi, M., & Ono, S. (2006). Aluminum substitution in stishovite and $MgSiO_3$ perovskite: High-resolution ^{27}Al NMR. *American Mineralogist*, *91*(2–3), 337–343. https://doi.org/10.2138/am.2006.1988

Wang, Y., Guyot, F., & Liebermann, R. C. (1992). Electron microscopy of (Mg, Fe)SiO_3 Perovskite: Evidence for structural phase transitions and implications for the lower mantle. *Journal of Geophysical Research*, *97*(B9), 12327. https://doi.org/10.1029/92JB00870

Xu, Y., & McCammon, C. (2002). Evidence for ionic conductivity in lower mantle (Mg,Fe)(Si,Al)O_3 perovskite. *Journal of Geophysical Research: Solid Earth*, *107*(B10), ECV 11-1-ECV 11-7. https://doi.org/10.1029/2001JB000677

Yates, J. R., Pickard, C. J., & Mauri, F. (2007). Calculation of NMR chemical shifts for extended systems using ultrasoft pseudopotentials. *Phys. Rev. B*, *76*, 24401.

Zhang, G. B., & Smyth, D. M. (1995). Defects and transport of the brownmillerite oxides with high oxygen ion conductivity — $Ba_2In_2O_5$. *Solid State Ionics*, *82*(3–4), 161–172. https://doi.org/10.1016/0167-2738(95)00196-2

Zhang, Y., & Xu, Z. (1995). Atomic radii of noble gas elements in condensed phases. *American Mineralogist*, *80*(7–8), 670–675.

Table 1. Al-bearing bridgmanite samples investigated in this study. Uncertainties on OV and CC contents are calculated from the microprobe analysis uncertainties reported in Table S3.

Starting materials	Synthetised products	Brg compositions	OV (mol%)	CC (mol%)
A ($En_{95}Brm_5$)	Brg	$Mg_{0.991}Al_{0.050}Si_{0.959}O_{2.984}$	3.2 (9)	0.9 (1)
B ($En_{90}Brm_{10}$)	Brg	$Mg_{0.975}Al_{0.100}Si_{0.925}O_{2.975}$	5.0 (8)	2.5 (5)
C ($En_{80}Brm_{20}$)	Brg + Per	$Mg_{0.937}Al_{0.161}Si_{0.902}O_{2.982}$	3.5 (7)	6.3 (4)
D ($En_{95}Cor_5$)	Brg	$Mg_{0.952}Al_{0.101}Si_{0.947}O_{2.998}$	0.5 (8)	4.8 (3)
E ($En_{75}Cor_{25}$)	Brg + Cor + trace Sti	$Mg_{0.884}Al_{0.235}Si_{0.881}O_{2.999}$	0.3 (7)	11.6 (4)
F *	Brg + Per	$Mg_{0.968}Al_{0.099}Si_{0.933}O_{2.983}$	3.5 (9)	3.2 (6)

Brm = $MgAlO_{2.5}$ (brownmillerite); Brg = bridgmanite; Cor = Al_2O_3; En = $MgSiO_3$; Per = periclase; Sti = stishovite

*The F starting material consisted of a mixture of 70 wt.% enstatite synthesized from glass D and 30 wt.% MgO

Table 2. Quantities (in %) of the ^{IV}Al, ^{V}Al, ^{VI}Al and ^{A}Al species assigned to the OV component and the CC component, respectively, and resulting OV/CC (%) ratio from the 1D ^{27}Al MAS NMR spectra. The OV/CC ratio obtained from the chemical compositions is reported for comparison.

Samples	**Al p.f.u.**	**^{IV}Al %**	**^{V}Al %**	**^{VI}Al % (OV / CC)**	**^{A}Al %**	**OV/CC NMR**	**OV/CC EPMA**
A	0.050	44	23	12 /11	11	79 (2) / 21 (2)	78 (7) / 22 (7)
B	0.100	22	21	17 / 20	20	60 (3) / 40 (3)	67 (4) / 33 (4)
C	0.161	9	9	23 / 29	29	41 (3) / 59 (3)	36 (6) / 64 (8)
D	0.101	2	3	5 / 45	45	10 (4) / 90 (4)	9 (12) / 91 (11)
E	0.235	--	--	-- / 50	50	0 (2) / 100 (2)	2 (4) / 98 (5)
F	0.099	10	9	22 / 30	30	41 (2) / 59 (2)	49 (8) / 51 (7)

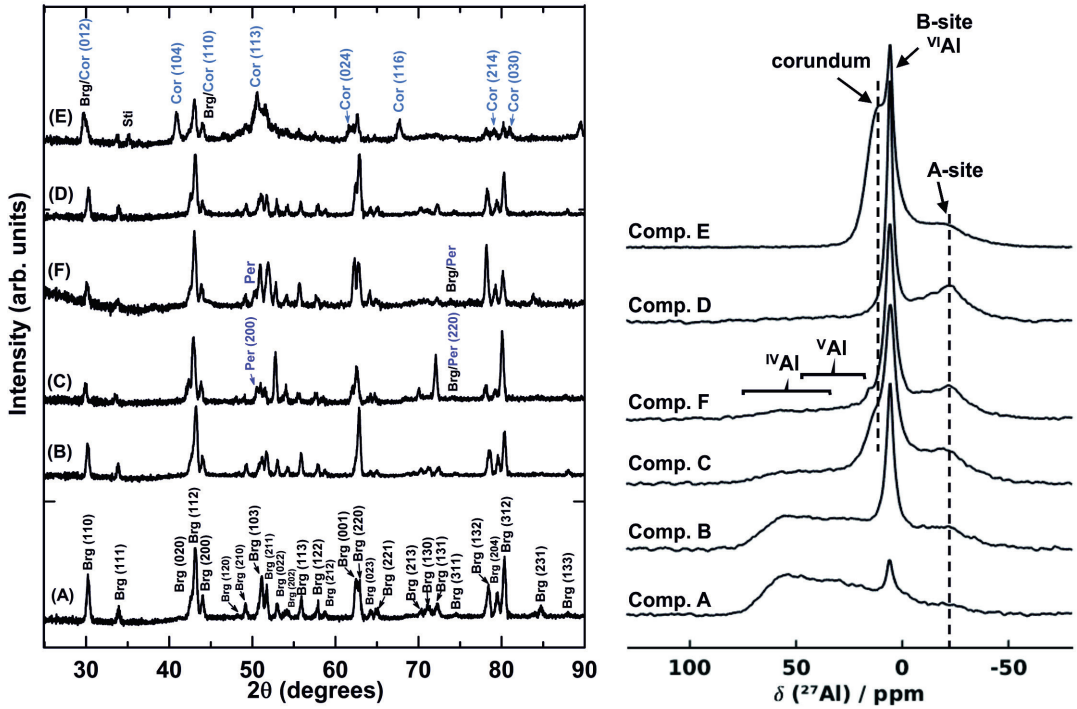

Fig. 1. **XRD (left) and ^{27}Al MAS NMR (right) spectra of Al-bearing bridgmanite samples.** Left: All samples are comprised predominantly of bridgmanite (Brg). In samples C and F bridgmanite coexists with periclase (Per) and sample E contains some corundum (Cor). Periclase does not contain any Al and, therefore, does not have an ^{27}Al NMR signature. Right: All ^{27}Al MAS NMR spectra exhibit resonances assigned to Al on the A and B sites of bridgmanite. Additionally, the spectra of sample A-C and F exhibit broad resonances in the typical shift range of tetra- (~50-80 ppm) and penta-coordinated (~25-55 ppm) Al species.

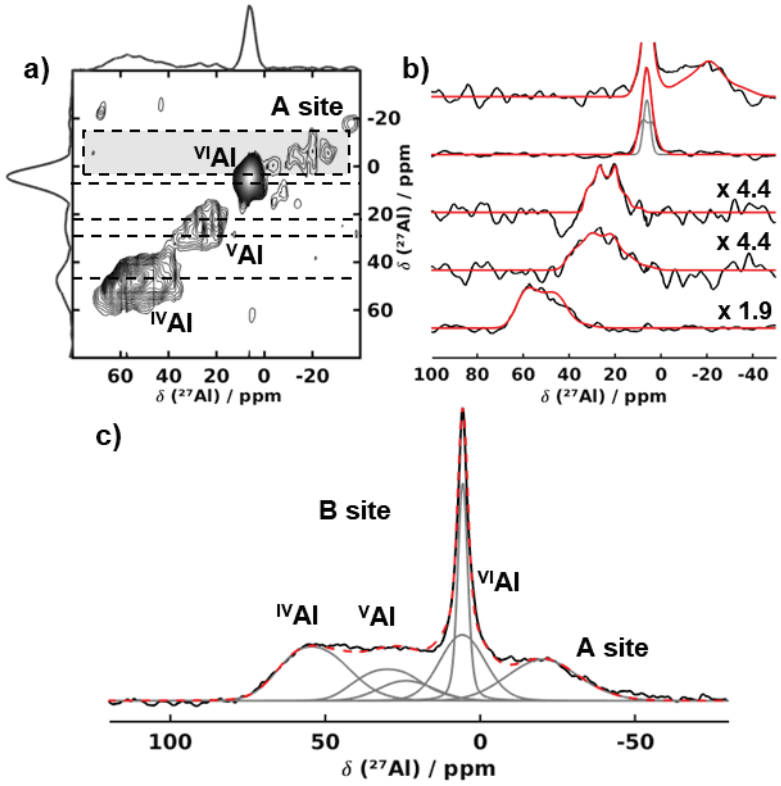

Fig. 2. (a) 2D ^{27}Al STMAS NMR spectrum, (b) profile fits of the 1D rows and (c) resulting refinement of the 1D ^{27}Al MAS NMR spectrum of sample B. (a) The 2D ^{27}Al STMAS NMR spectrum reveals four distinct Al environments typical for ^{IV}Al, ^{V}Al and ^{VI}Al in addition to Al on the A site of bridgmanite (^{A}Al). b) Profile fits (red) of the individual resonances for the 1D rows indicated by dashed lines and the grey shaded area in a). Relevant refinement parameters are given in Table S4. c) Refinement of the corresponding 1D ^{27}Al MAS NMR spectrum with resonances for ^{IV}Al, ^{V}Al, ^{IV}Al and ^{A}Al.

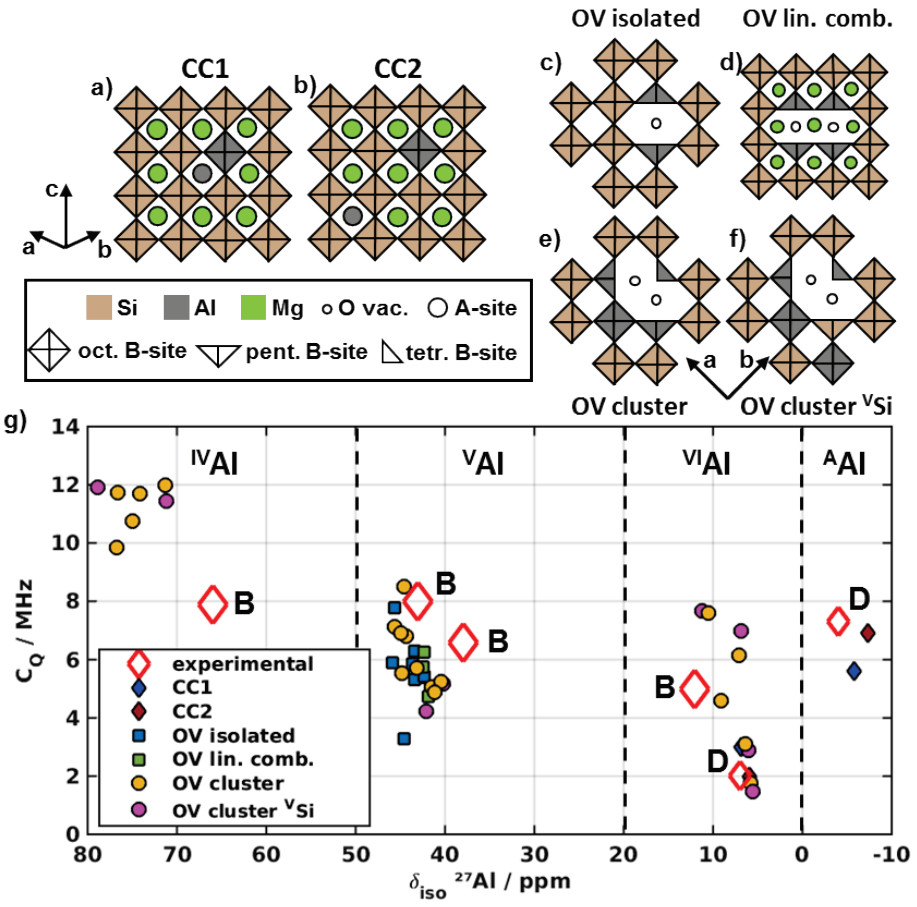

Fig. 3. (a-f) Schematic representations of Al defect models within bridgmanite and (g) corresponding calculated NMR parameters in comparison to the experimental observations. Examples of potential Al defect structures in bridgmanite for the CC (a, b) and the OV mechanism (c-f) and g) corresponding calculated quadrupolar coupling C_Q and isotropic chemical shift δ_{iso} of the Al defect sites in comparison to the experimental results of sample B and D. A detailed description of each Al defect model is given in the Supporting Information.

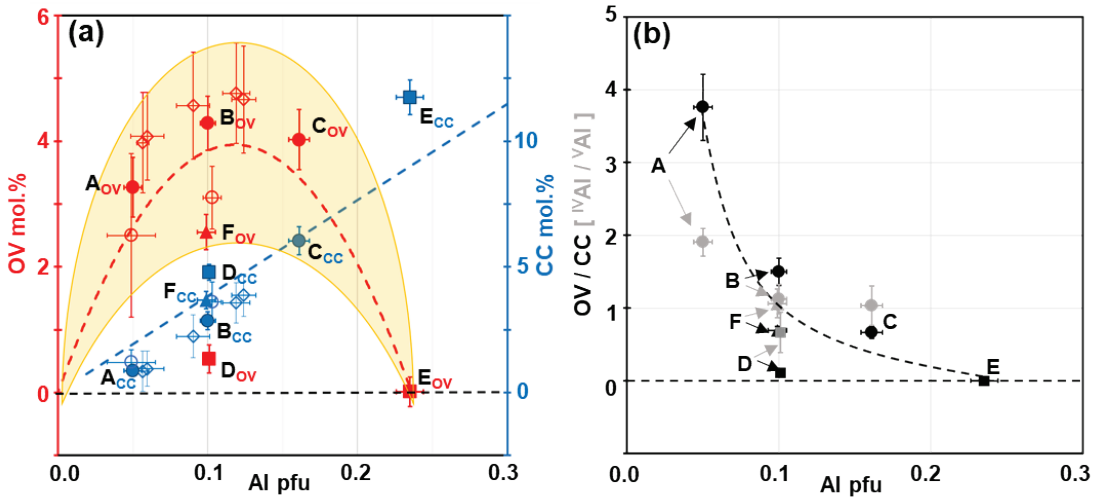

Fig. 4. (a) Proportions of OV and CC components and (b) OV/CC ratio determined by NMR spectroscopy. (a) Proportions of OV and CC substituted Al versus Al content (per formula unit) in bridgmanite in the systems $MgSiO_3$–$MgAlO_{2.5}$ (circles) and $MgSiO_3$–Al_2O_3 (squares) and in the reversal run F (triangle), in the present and previous studies. Solid symbols are the present study (Table S5), while the open circle and diamond symbols are data based on analyses of chemical composition from Kojitani et al. (2007) and Navrotsky et al. (2003). The yellow shading outlines the compositional range of the OV component. (b) Additionally to the OV / CC ratio (black) the $^{IV}Al/^{V}Al$ ratio (grey) determined from the refinement of the 1D ^{27}Al MAS NMR spectra (Table S5) of sample A to D is depicted.